PAN

Opto-Electronics Review

journal homepage: https://journals.pan.pl/opelre

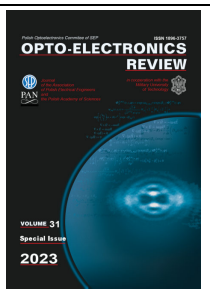

Multi-technique characterisation of InAs-on-GaAs wafers with circular defect pattern

Jacek Boguski[1*], Jarosław Wróbel[1], Sebastian Złotnik[1], Bogusław Budner[2], Malwina Liszewska[2], Łukasz Kubiszyn[3], Paweł P. Michałowski[4], Łukasz Ciura[5], Paweł Moszczyński[6], Sebastian Odrzywolski[1], Bartłomiej Jankiewicz[2], Jerzy Wróbel[1,7]

[1] Institute of Applied Physics, Military University of Technology, gen. Sylwestra Kaliskiego 2, 00-908 Warsaw, Poland
[2] Institute of Optoelectronics, Military University of Technology, gen. Sylwestra Kaliskiego 2, 00-908 Warsaw, Poland
[3] VIGO Photonics S.A., Poznańska 129/133, 05-850 Ożarów Mazowiecki, Poland
[4] Łukasiewicz Research Network-Institute of Microelectronics and Photonics, Al. Lotników 32/46, 02-668 Warsaw, Poland
[5] Department of Electronics Fundamentals, Rzeszów University of Technology, W. Pola 12, 35-959 Rzeszów, Poland
[6] Institute of Computer and Information Systems, Military University of Technology, gen. Sylwestra Kaliskiego 2, 00-908 Warsaw, Poland
[7] Institute of Physics, Polish Academy of Sciences, Al. Lotników 32/46, 02-668 Warsaw, Poland

Article info

Article history:
Received 17 Oct. 2022
Received in revised from 06 Dec 2022
Accepted 30 Dec. 2022
Available on-line 24 Feb. 2023

Keywords:
Wafer homogeneity; wafer defect pattern; surface roughness; indium arsenide; beryllium doping.

Abstract

The article presents the results of diameter mapping for circular-symmetric disturbance of homogeneity of epitaxially grown InAs (100) layers on GaAs substrates. The set of acceptors (beryllium) doped InAs epilayers was studied in order to evaluate the impact of Be doping on the 2-inch InAs-on-GaAs wafers quality. During the initial identification of size and shape of the circular pattern, non-destructive optical techniques were used, showing a 100% difference in average roughness between the wafer centre and its outer part. On the other hand, no volumetric (bulk) differences are detectable using Raman spectroscopy and high-resolution X-ray diffraction. The correlation between Be doping level and circular defect pattern surface area has been found.

1. Introduction

The "wafer homogeneity" test is often used as a good decent measure of the qualitative material growth character [1]. However, this term is difficult to define precisely [2] because of the multitude contexts of technological processes and measurements. These may result in local differences of electrical [3], optical [4], surface morphology and topography [5, 6], chemical composition [7], structure [8], temperature [9], and many other measurable parameters. In addition, a quantitative "result" of the homogeneity tests frequently depends on the arbitrarily adopted grid and its resolution in the measurement technique used. Therefore, more advanced approaches, supported by big data analytics and machine learning methods, have been used [10, 11]. There is a common agreement that the epitaxial structures homogeneity should be as high as possible at least on the device scale that one wants to produce. Generally, the larger area of the device structure, the greater the difficulty in controlling homogeneity during growth and crucial steps of processing [12, 13]. This is especially important in a production of detector arrays even for relatively thick layers [14, 15], and obviously a degree of difficulty in achieving high wafer homogeneity increases with a decrease of a layer thickness. In the case of monoatomic-like layer (so-called "2D materials"), there is a lack of efficient and stable approaches to the synthesis of thin films with a large area accompanied with excellent homogeneity [16, 17]. However, some impressive successes for few material systems have already been reported in this regard [18, 19].

*Corresponding author at: jacek.boguski@wat.edu.pl

https://doi.org/10.24425/opelre.2023.144564
1896-3757/ Association of Polish Electrical Engineers (SEP) and Polish Academic of Sciences (PAS). Published by PAS

For $A^{III}B^{V}$ semiconductor compounds, especially 6.1 Å-family materials, there has also been great progress in uniformity improvements and mapping techniques developments. Many recent research studies on thick layers of arsenides (e.g., InAs, GaAs), antimonides (e.g., InSb, GaSb), and their ternary alloys (e.g., $InAs_{1-x}Sb_x$) [20–23], as well as low-dimensional structures composed of aforementioned compositions, like quantum dots (QDs) [24–26], nanowires [27, 28], quantum-well infrared photodetectors (QWIPs) [29], or type-II superlattices (T2SLs) [30–32], indicate strong interest in the topic. Considering mapping, the aim is to obtain as much information as possible using non-destructive techniques. For this reason, the optical or semi-optical methods such as: high-resolution X-ray diffraction (HR-XRD) [24], photoluminescence (PL) [22, 24, 25, 30, 31, 33], local photocurrent mapping (LPM) [32, 34], spatially separated pump-probe (SSPP) spectra [21], lock-in thermography [20], scanning thermal microscopy (STM) [28] are mostly preferred. In many cases, however, contactless electric [35] or non-destructive tactile methods such as atomic force microscopy (AFM) [23] are also used. Unfortunately, in most of such studies, measurements are normally carried out for very small, selected areas, or the analysis is only qualitative for a full wafer scan. For this reason, sample preparation for destructive measurement techniques is sometimes needed [26, 29, 36]. In this work, the authors present both described approaches for a 2-inch epitaxially grown indium arsenide (InAs) undoped and intentionally Be-doped on GaAs substrates. First of all, non-destructive methods were implemented in order to determine basic surface and bulk parameters, and precisely select a large sub-area of homogeneity (LSAH) with systematic pattern. These observations seem to be a good complement to other interdisciplinary studies in the field of triboelectrochemical effects, in which one tries to find correlation between surface topography and electrochemical processes on the surface [37], including electrical field under contacts effects [38]. The authors are convinced that the presented research gives an insight on better understanding the parasitic effects in micro- and nanoelectronics composed of $A^{III}B^{V}$ semiconductor structures, for which p+ type InAs is often one of the sub-contact layers. It can also be very important in the development of plasmonic structures based on these materials [39, 40].

2. Experiment

2.1. Growth conditions

All InAs-on-GaAs (listed in Table 1) were grown in a RIBER Compact 21-DZ solid-source molecular beam epitaxy (MBE) system. Before each growth process, degassing of a GaAs substrate was performed for thermal desorption of oxides. A 250 nm thick GaAs buffer layer was initially grown with a 0.6 μm/h growth rate, to improve the substrate surface quality after degassing process. The InAs layers were grown with a ~0.4 μm/h growth rate at 450 °C. An acceptor concentration was controlled by temperature of a Be effusion cell. A manipulator rotation was set at 10 rpm during each growth. The specification of MBE system applied is described in more details elsewhere [41, 42].

Table 1.
The list of examined InAs on-GaAs.

Wafer no.	InAs layer thickness [μm]	Assumed Be concentration [cm^{-3}]
#1	5.15	-
#2	4.40	$1.0 \cdot 10^{16}$
#3	4.30	$5.0 \cdot 10^{16}$
#4	4.57	$1.0 \cdot 10^{17}$
#5	4.58	$5.0 \cdot 10^{17}$
#6	4.55	$1.0 \cdot 10^{18}$
#7	4.55	$5.0 \cdot 10^{18}$

2.2. Non-destructive wafers characterisation methods

Initial macroscopic assessment of morphological differences was conducted by an optical microscope (Nikon Eclipse LV 150N with active vibration isolation table). The morphology measurements of Be-doped InAs layers were performed using the NT-MDT atomic force microscope (AFM) in the intermittent contact mode. The measurements were conducted with the use of μMash measuring probes HQ: NSC15/AlBS with the following specification: resonance frequency of 325 kHz, force constant of 40N/m, tip radius approx. 8 nm. AFM was performed on 9 samples (5×5 mm each) cut along one line of the InAs-on-GaAs wafers; marked from A1 to A9 (see Fig. 1). During the measurements, the orientation of the X-Y samples and their order were kept as in the original wafer. Moreover, the measurements were made at 3 regions on each sample with the following coordinates: i) X = 2.50 mm, Y = 2.50 mm, ii) X = 0.85 mm, Y = 2.50 mm, and iii) X = 4.15 mm, Y = 2.50 mm. As a result, keeping the order of the samples, the measurements were taken along a straight line with a step of 1.65±0.05 mm. A scanning area was set at 30×30 μm. The selected area is optimal in terms of determining the surface roughness of samples and gives a good average roughness result and its repeatability. To estimate the accuracy of the obtained roughness parameters, the additional measurements and analysis of the repeatability of root mean square roughness (S_q) determination were performed. Five consecutive measurement probes were used to perform the measurements in the centre of the sample A2 and A5 and a total of 10 scans per sample were made. The conducted analysis allows to estimate the influence of parameters of the measuring probe (probe radius) on the roughness value, however, a strong influence of the measured structure dimensions on the determined standard deviation is also visible. For sample A2 with smaller structures, the relative measurement error calculated as the ratio of the standard deviation to the average roughness value is approximately 2.3%, while for sample A5, with higher and larger structures in the XY axes, this parameter is between 9.9% and 10.7%. The results obtained for sample A2 clearly show that the repeatability of measurements with the use of several measuring probes is very high. In the case of larger structures on sample A5, the roughness dispersion increases significantly, but it also depends on the boundaries of the measurement area (the repeatability of the measurement area in subsequent measurements was about ±20 μm).

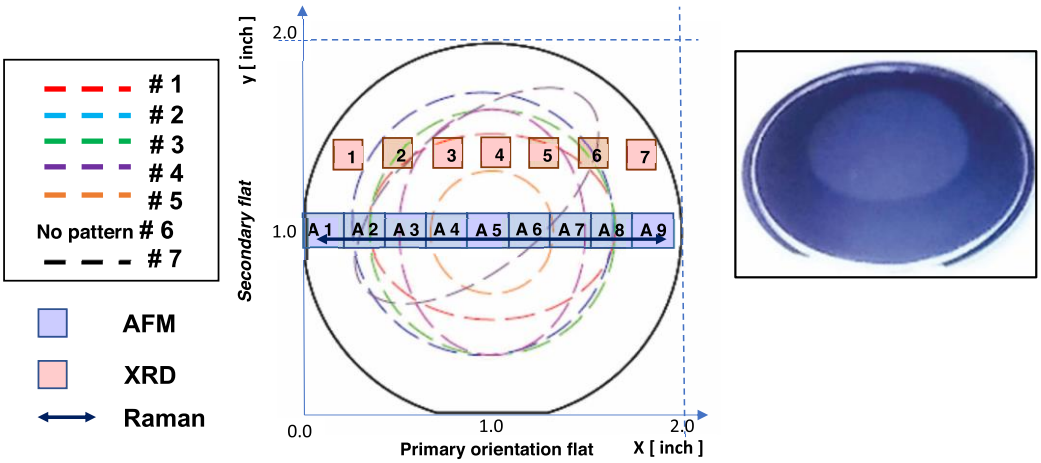

Fig. 1. The schematic arrangement of measurement lines and points for different measurement techniques performed on the InAs-on-GaAs wafer. Inset presents a photo of a real wafer with a circular shape surface pattern, visible sometimes under intense blue lighting and selected angle. The pattern borders are marked with a dashed line.

Consequently, for all measurements, it can be assumed that the maximum measurement error is at the level of 10.7%.

An HR-XRD analysis was performed using a PANalytical X'Pert MRD (Cu Kα1 radiation). The initial 2θ-ω scans for symmetric (004) have been performed [Fig. 5(a)] for a general verification of the crystallographic quality of the tested layers. Next, 2θ-ω scans and ω-scans for symmetric (004) and asymmetric (115) planes were recorded in seven separated spots marked in Fig. 1 – three centrally located in an internal texture, two others at a boundary of the identified textures and side ones in external texture for #3. Moreover, a full width at half maximum (FWHM) of (004) and (115) diffraction lines was estimated.

Raman spectra were carried out using a Renishaw inVia Reflex Raman microscope equipped with an EMCCD detector (Andor Technology Ltd, Oxford Instruments, Belfast, UK). The Raman signals were recorded in the spectral range of 18−1754 cm^{-1} with a 532 nm laser radiation coupled to an Eclipse filter (100 μm slit). The laser excitation power was ca. 20 mW on the sample. The laser beam was directed to the sample through a 20x (N.A. = 0.4) objective lens from Leica. A 15 s integration time and a 25 s accumulation time at point were applied. Raman spectra were measured along the wafer diameter (2 lines) with a step of 0.5 mm in air and at room temperature. The wavelength of the instrument was calibrated using an internal silicon wafer, the spectrum was centred at 520.5 cm^{-1}. Collected Raman spectra were processed in a WiRE 5.4 software.

2.3. Destructive wafers characterisation methods

Secondary ion mass spectrometry (SIMS) depth profiles were performed using a CAMECA SC Ultra instrument under ultra-high vacuum (UHV), usually of $4 \cdot 10^{-10}$ mbar. Cs^+ primary beam rastered over 80×80 μm^2 (the analysis area was limited to 40×40 μm^2) and positive ions detection mode was used for detection of Be. SIMS analysis was performed to evaluate in-depth Be content in InAs layers.

3. Results and discussion

The central circular pattern, often visible in a blue light, is common in mass production [12] and, therefore, it is sometimes called "a circle defective wafer bin map" [43]. Its presence might be related to the release of defects from nonideal substrate or might result from the method of wafer surface polishing [44]. The heterogeneous stress distribution during mechanical planarization [45] or temperature distribution during this process [46] may also play a role. The circular shape of a pattern probably results from the lack of perfect flat parallelism of the wafer, which in turn affects the heat flows [47] or reflects difficulties in uniform heating of the wafer in the growth reactor [48]. In addition, wafer bowing, connected with different growth conditions might have an impact on the wavelength homogeneity [49] or uniformity of the particle streams during growth [50].

In this work, the authors did not focus on the identification of the exact source of such "defective circle". Instead, they performed the number of local tests and measurements, as listed in Fig. 1 legend, to correlate positions on the wafer with bulk and surface properties of the underlying InAs epilayer. In Fig. 1, the boundaries of defect patterns areas (dashed lines) and the measurement areas have been marked (light brown rectangles for XRD measurements, blue rectangles for AFM analysis, arrow along the diameter parallel to the primary orientation flat for the Raman spectroscopy analysis).

3.1. Non-destructive characterisation

3.1.1. Surface disturbance

Primarily, the textures, which are visible across the wafer, were examined using optical microscope (Fig. 2) and AFM imaging (Fig. 3). From the photos shown in Fig. 2, it is evident that surface texture changes across the wafer as it approaches the dashed borderline (marked in Fig. 1).

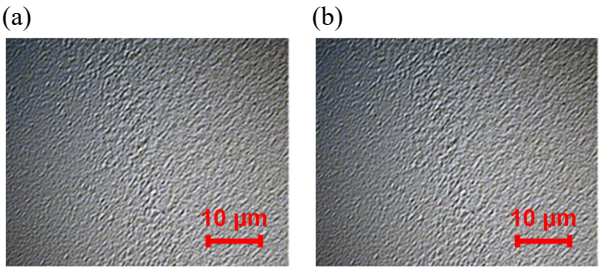

Fig. 2. The high-resolution photos taken for the outside (a) and inside (b) of the circular defect pattern for #3 (Table 1). Brightness and contrast were selected automatically.

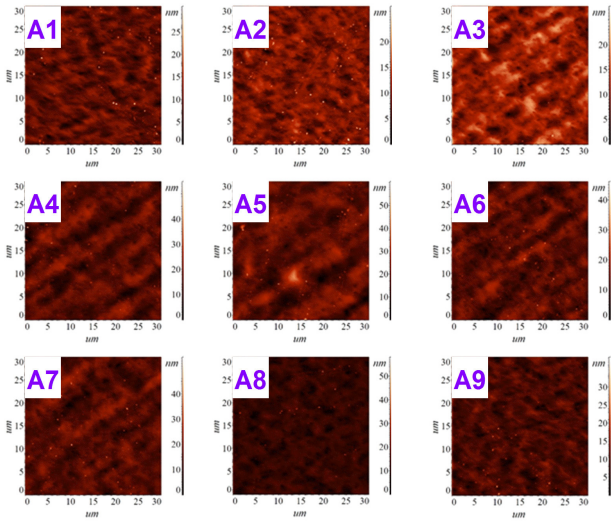

Fig. 3. Surface topography recorded with an AFM microscope at the centre of 9 samples cut from the tested wafer (#3). Consecutive samples A1 to A9 are named according to the numbering shown in Fig. 1.

Moreover, the surface textures are slightly different on the opposite sides of the inner circle. Therefore, the common mapping process, which is taken from the centre along the radius towards one edge only, would be insufficient to obtain an overall overview of the investigated wafer. To further emphasize this point, the authors performed detailed tests using the AFM technique. Surface micrographs were taken along the wafer diameter, which was parallel to the primary flat. Results obtained at equally spaced points (A1 to A9, see Fig. 1) are shown in Fig. 3.

It is observed that morphology features at positions (A1, A2) and (A8, A9) are very similar to each other and that their size is smaller as compared to other locations. It is evident, that the size of these features, formed during the deposition on the GaAs wafer, increases when moving from the edges to the centre of the wafer, in agreement with optical photos. Interestingly, the AFM micrographs in the sequence of A3–A7 clearly show that the features are ordered from the lower-left to the upper-right corner. Therefore, inner parts of the wafer do not exhibit the circular symmetry, which is quite unexpected, but might be related to a 2° offcut of the GaAs substrate.

Figure 3 also shows that a periodic micro-faceting of a surface (similar to "step bunching" effect) in the inner part of the wafer is not only diagonally ordered but also enlarged comparing to near-edge randomly distributed features. From AFM data, S_q parameter for different locations across diameter was calculated; the results are shown in Fig. 4.

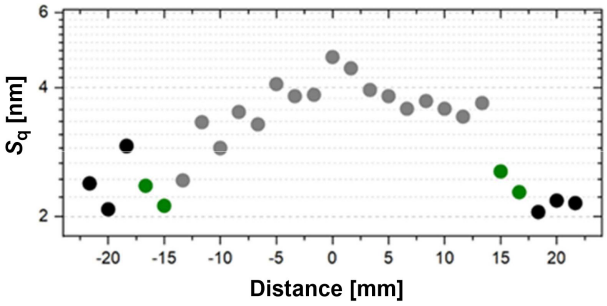

Fig. 4. Root mean square roughness S_q as a function of the position on the wafer diameter (distance from the wafer centre) for the #3.

The obtained area with the highest S_q values (grey dots) correlates with the roughly defined texture boundary observed using the optical microscopy. The maximum value of S_q is 4.7 nm at 0 position, with error estimated to be approx. 10%. For comparison, S_q value for an homoepitaxially grown InAs on InAs (100) substrate under similar growth conditions is one order of magnitude lower −0.19 m [51]. It is clearly observed that, the determined S_q parameters are evidently the smallest close to the wafer edges. The observed slight variability in S_q values is the result of a rigid selection of the measurement grid sub-areas. Some certain randomness in the appearance of a dust spot has been minimized by numerically removing small sub-areas of extremely large sizes.

3.1.2. Bulk properties

The important question arises, whether the observed surface morphology is correlated with bulk properties of InAs epilayers. To answer it, the authors performed a series of HR-XRD scans for each wafer [centre of wafers, Fig. 5(a)] and at positions marked with light brown rectangles in Fig. 1, for #3 [Figs. 5(b) and (c)]. The authors also collected Raman spectra maps for the same locations as probed with AFM (A1–A9 range, blue rectangles – Fig. 1), for #3.

Figure 5(a) shows no essential differences in diffractograms between wafers with different Be doping level. In order to be more precise, a deeper XRD analysis of the #3 was performed along its diameter parallel to the primary orientation flat, for 9 rectangular areas marked in Fig. 1. The results of the analysis are shown in Fig. 5(b). In this figure, a set of XRD results solely for symmetrical (004) diffraction lines and estimated FWHM of (004) and (115) from aforementioned measurement areas is shown. The XRD results reveal sharp and overlapped peaks, proving an abruptness of p-InAs interface with underlayers and uniformity across the wafer. On the other hand, FWHM of a layer peak can be used to qualitatively compare the crystal quality, associated with threading defect density (dislocations), mosaic domain or wafer curvature, as long as the samples share identical structure and are measured using the same XRD instrument and conditions [52]. The average FWHM ω values with standard deviations are 167.4±2.5 and 159.4±2.2 arcsec for (004) and (115) reflections, respectively [Fig. 5(c)]. The obtained ω FWHM of (004) are consistent with a previously reported InAs grown on (001)-oriented GaAs [42, 53], while FWHM

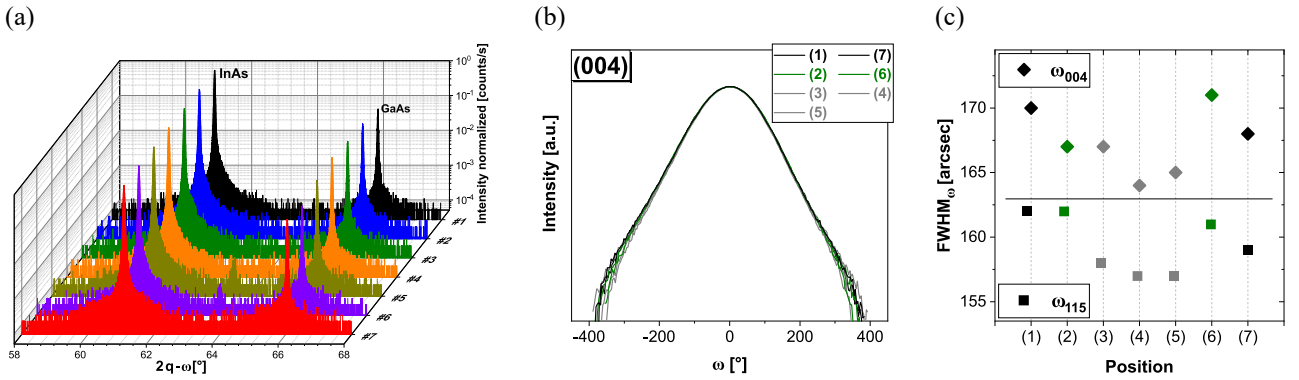

Fig. 5. A list of X-ray diffractograms on 2 Theta–Omega angle at the centre of each wafer in form of a 3D collection chart (a); XRD ω-scans of the (004) InAs reflections measured across the 2-inch wafers in seven spots marked in Fig. 1(b); FWHM of (004) and (115) estimated from the aforementioned areas (c).

ω (115) is much lower than reported for InAs on (111) GaAs and (111) GaSb [52]. In conclusion, these XRD datasets demonstrate slight broadening across the wafer with the lowest FWHM values at the centre. Nevertheless, a difference of approx. 5 arcsec can be neglected, indicating in overall a good film quality and high homogeneity.

The lack of correlation between structural quality and surface roughness was supported by Raman spectral mapping [54], shown in Fig. 6(a)–(c). This type of Raman measurements of large sample areas, performed for determination of their homogeneity, are rarely described in the literature [23, 55].

The representative Raman spectra recorded at distinct spots are shown in Fig. 6(a). The most intense peak at 230.3 cm^{-1} corresponds to the longitudinal optical (LO) phonons from the top strain-free InAs layer. The double transverse acoustic (2TA) band at 105.2 cm^{-1} corresponds to the second-order Raman scattering by acoustic phonons of bulk InAs. The second-order peaks and combinational modes, which are related to optical and acoustic phonons, appear in the spectrum in the range of 415–485 cm^{-1}. All the mentioned Raman bands indicate the high quality of the sample [42, 56–58]. The changes of 2TA and LO bands positions and normalised intensities across the wafer diameter are shown in Figs. 6(b) and 6(c), respectively. The position of 2TA peak and its intensity are constant across the entire diameter of the wafer. It proves again a high structural quality and bulk homogeneity of the epilayer. Moreover, there are no additional peaks in the entire Raman spectrum range, which proves the high chemical purity of the samples [59–61]. Small fluctuations of the intensity in the LO peak are attributed to the laser stability, which generally may not be perfect for long-lasting measurements [62].

3.2. *Destructive characterisation*

Finally, the SIMS measurement for each wafer was performed (Fig. 7). It is clearly detectable that Be concentration is rather constant across the layers, proving that the intentional Be dopant is well distributed. However, there is a slight difference between assumed content (dash lines) and real concentration (SIMS results). In all cases, the ratio of the real Be content to the assumed one in the growth varies between 1.51 and 1.13, being the smallest for the highest Be concentration ($5 \cdot 10^{18}$ cm^{-3}). These results indicate a constant Be distribution across the layers.

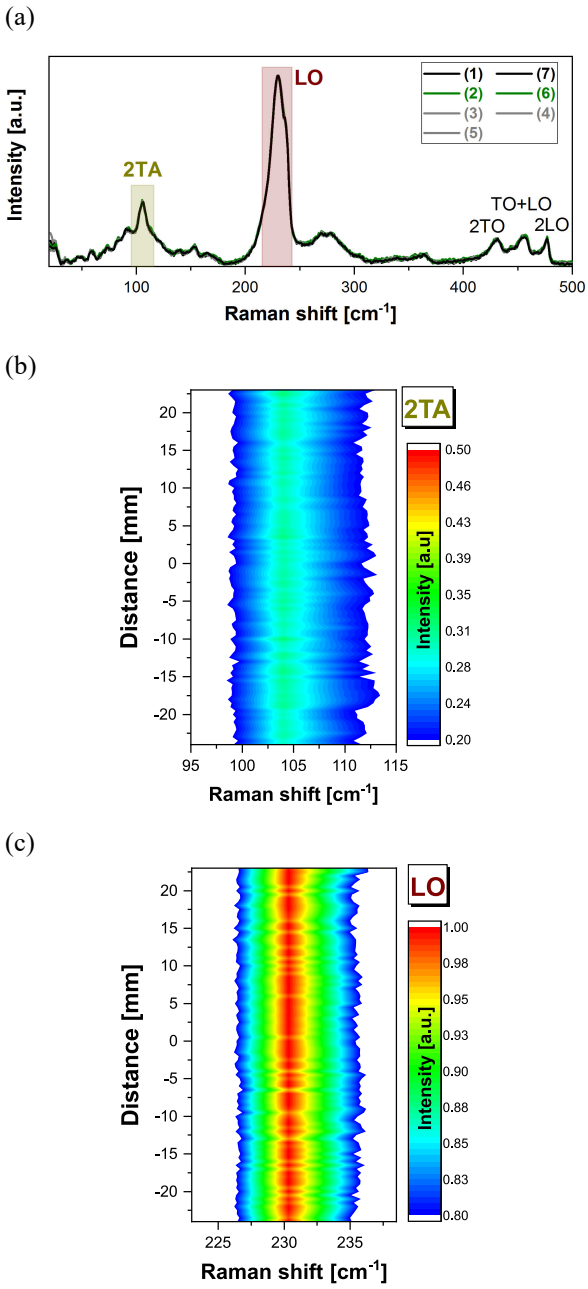

Fig. 6. Intensity *vs*. Raman shift obtained at seven points, as indicated in Fig. 1(a), for #3. Diameter scans of the normalized Raman spectra for 2TA and LO bands, respectively (b)–(c).

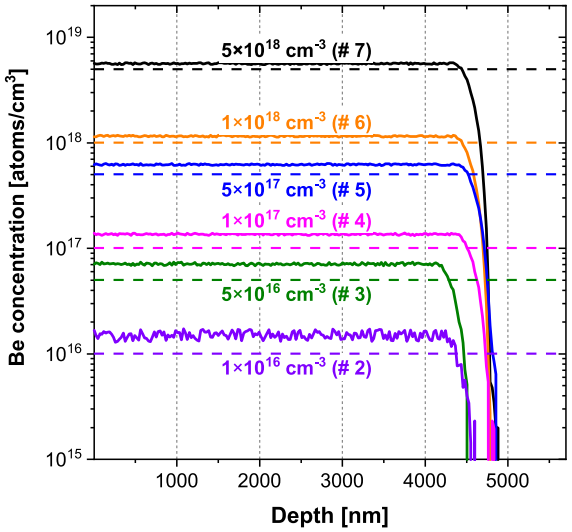

Fig. 7. SIMS spectrum of Be content for each layer (solid lines) *vs*. assumed Be content from the MBE process parameters applied.

Regarding the SIMS data, a correlation between the designated surfaces of the circular defect areas and the concentration of Be was carried out (Fig. 8).

It should be stated that there is a downward trend in defect pattern area *vs*. Be concentration in the range of $1 \cdot 10^{16}$ and $1 \cdot 10^{18}$ cm^{-3}. Results above this range significantly deviate from the observed trend. This may be due to the abrupt change in electrical properties for that Be concentration for which the layer under investigation acquires metallic properties. Taking into account the even distribution of Be deep into the layer (Fig. 7), it can be assumed that, in this case, deviation from the observed trend may be due to surface phenomena. Possibly, an in-depth examination of the layers for their electrical properties could explain these observations. However, it will be a challenge for the future.

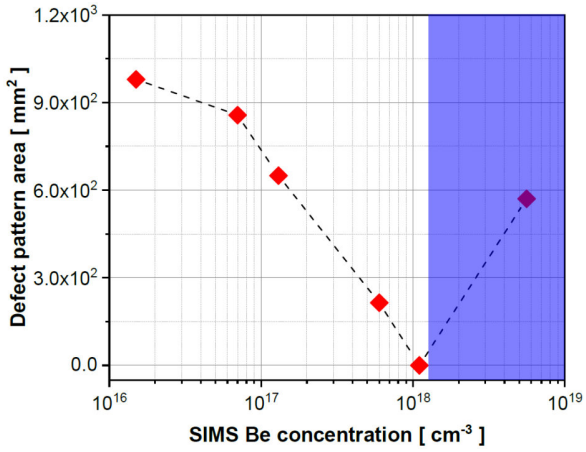

Fig. 8. A correlation between circular defect pattern areas and SIMS Be concentration for the wafers examined.

4. Conclusions

The XRD and Raman spectroscopy mapping results show no noticeable differences in the wafer volume regardless of the position along the diameter. This means that the observed texture distortion is only a surface effect. The homogeneous distribution of impurities in the in-depth profile eliminates other potential volumetric effects. The inner texture of the wafer surface has a roughness of about 100% greater than the outer texture. Additionally, the inner one seems to be more directional. It should be noted that only the results of the SIMS analysis allowed to determine the correlation between the level of Be doping and the surface of the observed defect patterns. The conclusions from the discussion allow for a hypothesis that the uneven distribution of heat during the MBE epitaxial growth may be responsible for the presence of these defects. It can be proved by a decreasing tendency of the determined correlation. The increasing concentration of acceptors increases the electrical conductivity, and, therefore, also increases the thermal conductivity. The performance of thermal conductivity tests at the epitaxial growth temperature (450 °C) would allow for the verification of the hypothesis.

Authors' statement

J.B.: conceptualization, investigation, writing – original draft; Ja.W.: conceptualization, methodology, project administration, writing – original draft, funding acquisition; S.Z.: data curation, investigation, visualization, writing – original draft; B.B.: data curation, formal analysis, investigation, writing – original draft. M.L.: investigation, writing – original draft; Ł.K.: investigation, resources; P.P.M.: data curation, formal analysis; Ł.C.: data curation, formal analysis; P.M.: data curation; S.O.: data curation, visualization; B.J.: resources, writing – review and editing; Je.W.: supervision, writing – review and editing.

Acknowledgements

This work has been completed with the financial support under the program of the Ministry of Education and Science (MEiN): "Regional Initiative of Excellence" in 2019-2022; project no. 014/RID/2018/19. funding amount of 4 589 200.00 PLN.

The authors would also like to thank Professor Józef Piotrowski from VIGO Photonics S.A. for the fruitful discussion.

References

[1] Mackenzie, D. M. A. *et al*. Wafer-scale graphene quality assessment using micro four-point probe mapping. *Nanotechnology* **31**, 225709 (2020). https://doi.org/10.1088/1361-6528/ab7677

[2] Jung, J.-R. & Yum, B.-J. Uniformity and signal-to-noise ratio for static and dynamic parameter designs of deposition processes. *Int. J. Adv. Manuf. Technol.* **54**, 619–628 (2011). https://doi.org/10.1007/s00170-010-2957-z

[3] Yager, T., Lartsev, A., Yakimova, R., Lara-Avila, S. & Kubatkin, S. Wafer-scale homogeneity of transport properties in epitaxial graphene on SiC. *Carbon* **87**, 409–414 (2015). http://doi.org/10.1016/j.carbon.2015.02.058

[4] El Harrouni, I., Bluet, J. M., Ziane, D., Sartel, C. & Guillot, G. Microscopic defects and homogeneity investigations in 4H-SiC epitaxial wafers by UV scanning photoluminescence spectroscopy. *Eur. Phys. J. Appl. Phys.* **27**, 235–238 (2004). https://doi.org/10.1051/epjap:2004105

[5] Xu, Z. L., Xu, X. P., Cui, C. C. & Huang, H. A new uniformity coefficient parameter for the quantitative characterization of a textured wafer surface and its relationship with the photovoltaic conversion efficiency of monocrystalline silicon cells. *Sol. Energy* **191**, 210–218 (2019). https://doi.org/10.1016/j.solener.2019.08.028

[6] Lee, J. L. S., Gilmore, I. S., Seah, M. P. & Fletcher, I. W. Topography and field effects in secondary ion mass spectrometry – Part I: conducting samples. *J. Am. Soc. Mass. Spectrom.* **22**, 1718–1728 (2011). https://doi.org/10.1007/s13361-011-0201-1

[7] Shojaei, B. *et al*. Full-wafer strain and relaxation mapping of $Hg_{1-x}CdxTe$ multilayer structures grown on $Cd_{1-y}ZnyTe$ substrates. *J. Electron. Mater.* **48**, 6118–6123 (2019). https://doi.org/10.1007/s11664-019-07289-1

[8] Knehr, E. *et al*. Wafer-level uniformity of atomic-layer-deposited niobium nitride thin films for quantum devices. *J. Vac. Sci. Technol. A* **39**, 052401 (2021). https://doi.org/10.1116/6.0001126

[9] Shimizu, E., Sugawara, S. & Nakata, H. Computational analysis of wafer temperature non-uniformity in MOVPE system. *J Cryst. Growth* **266**, 340–346 (2004). https://doi.org/10.1016/j.jcrysgro.2004.02.064

[10] Koo, J. & Hwang, S. A unified defect pattern analysis of wafer maps using density-based clustering. *IEEE Access* **9**, 78873–78882 (2021). https://doi.org/10.1109/Access.2021.3084221

[11] Hsu, C. Y., Chen, W. J. & Chien, J. C. Similarity matching of wafer bin maps for manufacturing intelligence to empower Industry 3.5 for semiconductor manufacturing. *Comput. Ind. Eng.* **142**, 106358 (2020). https://doi.org/10.1016/j.cie.2020.106358

[12] Dunn, T., Lee, C., Tronolone, M. & Shorey, A. Metrology for Characterization of Wafer Thickness Uniformity During 3DS-IC. in *2012 IEEE 62nd Electronic Components and Technology Conference (ECTC)* 1239–1244 (2012). https://doi.org/10.1109/ECTC.2012.6248993

[13] Nagano, M., Mitani, T., Ueda, K., Zettsu, N. & Yamamura, K. Improvement of thickness uniformity of bulk silicon wafer by numerically controlled local wet etching. *J. Cryst. Growth* **311**, 2560–2563 (2009). https://doi.org/10.1016/j.jcrysgro.2009.01.131

[14] Rogalski, A., Antoszewski, J. & Faraone, L. Third-generation infrared photodetector arrays. *J. Appl. Phys.* **105**, 091101 (2009). https://doi.org/10.1063/1.3099572

[15] Rogalski, A. *Infrared and Terahertz Detectors*. *Third Edition.* (CRC Press, Boca Raton, 2019). https://doi.org/10.1201/b21951

[16] Dai, T. J. *et al*. Synthesis of few-layer 2H-MoSe2 thin films with wafer-level homogeneity for high-performance photodetector, *Nanophotonics* **7**, 1959–1969 (2018). https://doi.org/10.1515/nanoph-2018-0153

[17] Shi, M. L. *et al*. Top-down integration of molybdenum disulphide transistors with wafer-scale uniformity and layer controllability. *Small* **13**, 1603157 (2017). https://doi.org/10.1002/smll.201603157

[18] Zhang, T. B. *et al*. High performance few-layer MoS2 transistor arrays with wafer level homogeneity integrated by atomic layer deposition. *2d Mater.* **5**, 5015028 (2018). https://doi.org/10.1088/2053-1583/aa9ea5

[19] Kang, K. *et al*. High-mobility three-atom-thick semiconducting films with wafer-scale homogeneity. *Nature* **520**, 656–660 (2015). https://doi.org/10.1038/nature14417

[20] Pawlak, M., Ramza, K. & Streza, M. Simultaneously mapping of in-depth thermal diffusivity and effective infrared absorption coefficient of silicon-doped gallium arsenide wafer using lock-in thermography. *Anal. Lett.* **52**, 93–101 (2019). https://doi.org/10.1080/00032719.2017.1405966

[21] Yeh, T. T. *et al*. Photoexcited carrier and phonon morphology of InSb observed with an ultrafast pump-probe microscope. *J Opt.* **23**, 074004 (2021). https://doi.org/10.1088/2040-8986/ac05d0

[22] Chen, X. R., Zhu, L. Q. & Shao, J. Spatially resolved and two-dimensional mapping modulated infrared photoluminescence spectroscopy with functional wavelength up to 20 um. *Rev. Sci. Instrum.* **90**, 093106 (2019). https://doi.org/10.1063/1.5111788

[23] Pal, S. *et al*. Self-catalyst assisted and catalyst-free epitaxial growth of InAs on Ge (111): Role of substrate surface and evolution of polytypism. *J. Vac. Sci. Technol. A* **35**, 061501 (2017). https://doi.org/10.1116/1.4996104

[24] Abouzaid, O. O-band emitting InAs quantum dots grown by MOCVD on a 300 mm Ge-buffered Si (001) substrate. *Nanomaterials* **10**, 2450 (2020). https://doi.org/10.3390/nano10122450

[25] Tatsugi, S., Sugiyama, R. & Yamaguchi, K. Photoluminescence Mapping Analysis of In-Plane Ultrahigh-Density InAs/GaAsSb Quantum Dot Layers. in *2019 Compound Semiconductor Week (CSW)* 112–113 (2019). http://toc.proceedings.com/49884webtoc.pdf

[26] Selvidge, J. *et al*. Non-radiative recombination at dislocations in InAs quantum dots grown on silicon. *Appl. Phys. Lett.* **115**, 131102 (2019). https://doi.org/10.1063/1.5113517

[27] Aseev, P. Selectivity map for molecular beam epitaxy of advanced III-V quantum nanowire network. *Nano Lett.* **19**, 218–227 (2019). https://doi.org/10.1021/acs.nanolett.8b03733

[28] Konemann, F. *et al*. Nanoscale Scanning Probe Thermometry. in *2018 24th International Workshop on Thermal Investigations of ICs and Systems (Therminic)* 1–6 (2018). https://doi.org/10.1109/THERMINIC.2018.8593312

[29] Santos, T. G. *et al*. Effect of electric field non-uniformity on the differences between I-V characteristics of QWIP devices fabricated on the same wafer. *Sens. Actuator A Phys.* **301**, 111725 (2020). https://doi.org/10.1016/j.sna.2019.111725

[30] Chen, X. R. *et al*. Modulated photoluminescence mapping of long-wavelength infrared InAs/GaSb type-ii superlattice: in-plane optoelectronic uniformity. *Phys. Rev. Appl.* **15**, 044007 (2021). https://doi.org/10.1103/PhysRevApplied.15.044007

[31] Kwan, D. C. M. Optical and structural investigation of a 10 um InAs/GaSb type-II superlattice on GaAs. *Appl. Phys. Lett.* **118**, 203102 (2021). https://doi.org/10.1063/5.0045703

[32] Meng, C. X. *et al*. Investigation of a noise source and its impact on the photocurrent performance of long-wave-infrared InAs/GaSb type-II superlattice detectors. *Opt Express* **28**, 14753–14761 (2020). https://doi.org/ 10.1364/Oe.386920

[33] Dyksik, M. *et al*. Submonolayer uniformity of type II InAs/GaInSb w-shaped quantum wells probed by full-wafer photoluminescence mapping in the mid-infrared spectral range. *Nanoscale Res. Lett.* **10**, 402 (2015). https://doi.org/10.1186/s11671-015-1104-z

[34] Rouis, W. *et al*. Local photocurrent mapping of InAs/InGaAs/GaPts intermediate-band solar cells using scanning near-field optical microscopy. *Sol. Energy Mater. Sol. Cells* **144**, 324–330 (2016). https://doi.org/10.1016/j.solmat.2015.09.026

[35] Stibal, R., Müller, S. & Jantz, W. Topographic electrical characterization of semi-insulating GaAs, InP and SiC substates. in *Compound Semiconductor Manufacturing Expo (CS-MAX)* 235–237 (2002).

[36] Sugiyama, H., Teranishi, A., Suzuki, S. & Asada, M. High-uniformity InP-based resonant tunneling diode wafers with peak current density of over 6 x 10(5) A/cm(2) grown by metal-organic vapor-phase epitaxy. *J Cryst. Growth* **336**, 24–28 (2011). https://doi.org/10.1016/j.jcrysgro.2011.09.010

[37] Joo, S. & Liang, H. In Situ characterization of triboelectrochemical effects on topography of patterned copper surfaces. *J. Electron. Mater.* **42**, 979–987 (2013). https://doi.org/10.1007/s11664-013-2486-2

[38] Zhang, P. Effects of Surface Roughness on Electrical Contact, RF Heating and Field Enhancement. (The University of Michigan, 2012). https://deepblue.lib.umich.edu/bitstream/handle/2027.42/95929/umpeng_1.pdf?sequence=1

[39] Naik, G. V., Shalaev, V. M. & Boltasseva, A. Alternative plasmonic materials: beyond gold and silver. *Adv. Mater.* **25**, 3264–3294 (2013). https://doi.org/10.1002/adma.201205076

[40] Wu, J. *et al*. Photoluminescence plasmonic enhancement in InAs quantum dots coupled to gold nanoparticles. *Mater. Lett.* **65**, 3605–3608 (2011). https://doi.org/10.1016/j.matlet.2011.08.019

[41] Benyahia, D. *et al*. Molecular beam epitaxial growth and characterization of InAs layers on GaAs (001) substrate. *Opt. Quantum Electron.* **48**, 428 (2016). https://doi.org/10.1007/s11082-016-0698-4

[42] Wróbel, J. *et al*. Structural and optical characterization of the high quality Be-doped InAs epitaxial layer grown on GaAs substrate. *Proc. SPIE* **10830**, 108300S (2018). https://doi.org/10.1117/12.2503624

[43] Lim, M. & Bae, S. J. Spatial monitoring of wafer map defect data based on 2D wavelet spectrum analysis. *Appl. Sci*. **9**, 5518 (2019). https://doi.org/10.3390/app9245518

[44] van der Velden, P. Chemical mechanical polishing with fixed abrasives using different subpads to optimize wafer uniformity. *Microelectron. Eng.* **50**, 41–46 (2000). https://doi.org/10.1016/S0167-9317(99)00262-2

[45] Park, J., Hong, S., Lee, S., Jin, Y. & Kim, T. Investigation of step structure in CMP retainer ring to improve within-wafer non-uniformity. *J. Mech. Sci. Technol.* **33**, 3391–3395 (2019). https://doi.org/10.1007/s12206-019-0634-1

[46] Lee, K., Lee, D., Jeong, S., Lee, D. & Jeong, H. Effect of spray nozzle position on pad temperature distribution and wafer non-uniformity. *J. Mech. Sci. Technol.* **33**, 5677–5682 (2019). https://doi.org/10.1007/s12206-019-1110-7

[47] Ramanan, N., Kozman, A. & Sims, J. B. On the differences between wafer and bake plate temperature uniformity in proximity bake: A theoretical and experimental study. *Proc. SPIE* **3999**, 890–898 (2000). https://doi.org/10.1117/12.388375

[48] Li, Z. M. *et al*. Temperature uniformity of wafer on a large-sized susceptor for a nitride vertical MOCVD reactor. *Chin. Phys. Lett.* **29**, 030701 (2012). https://doi.org/10.1088/0256-307x/29/3/030701

[49] Hoffmann, V. *et al*. Uniformity of the wafer surface temperature during MOVPE growth of GaN-based laser diode structures on GaN and sapphire substrate. *J. Cryst. Growth* **315**, 5–9 (2011). https://doi.org/10.1016/j.jcrysgro.2010.09.048

[50] Hardtdegen, H. *et al*. On the influence of gas inlet configuration with respect to homogeneity in a horizontal single wafer MOVPE reactor. *J. Cryst. Growth* **223**, 15–20 (2001). https://doi.org/10.1016/S0022-0248(00)00969-6

[51] Ye, H. *et al*. MBE growth optimization of InAs (001) homoepitaxy. *J. Vac. Sci. Technol. B* **31**, 03C135 (2013). https://doi.org/10.1116/1.4804397

[52] Ohtake, A., Mano, T. & Sakuma, Y. Strain relaxation in InAs heteroepitaxy on lattice-mismatched substrates. *Sci. Rep.* **10**, 4606 (2020). https://doi.org/10.1038/s41598-020-61527-9

[53] Benyahia, D. *et al*. Molecular beam epitaxial growth and characterization of InAs layers on GaAs (001) substrate, *Opt. Quantum Electron.* **48**, 428 (2016). https://doi.org/10.1007/s11082-016-0698-4

[54] Geurts, J. The characterization of semiconductor layer and interface quality with special reference to Raman spectroscopy. *Prog. Cryst. Growth Charact. Mater.* **32**, 185–224 (1996). https://doi.org/10.1016/0960-8974(96)00003-4

[55] Feng, Z. C. *et al*. Optical characterization and mapping of four-inch InSb epitaxial thin films grown on GaAs by turbo disk metalorganic chemical vapor deposition. *MRS Online Proc. Library Archive* **450**, 61–66 (1997). https://doi.org/10.1557/PROC-450-61

[56] Carles, R., Saint-Cricq, N., Renucci, J. B., Renucci, M. A. & Zwick, A. Second-order Raman scattering in InAs. *Phys. Rev. B* **22**, 4804–4815 (1980). https://doi.org/10.1103/PhysRevB.22.4804

[57] Tenne, D. A. *et* al. Raman study of self-assembled GaAs and AlAs islands embedded in InAs. *Phys. Rev. B* **61**, 13785–13790 (2000). https://doi.org/10.1103/PhysRevB.61.13785

[58] Grodecki, K., Murawski, K., Michalczewski, K., Jankiewicz, B. & Martyniuk, P. InAsSb mole fraction determination using Raman low energy modes. *Opt. Mater. Express* **10**, 149–154 (2020). https://doi.org/10.1364/OME.10.000149

[59] Vorlíček, V., Železný, V., Tiwari, A. N., Krejci, M. & Zogg, H. Determination of the crystallographic orientation of CuInSe2 thin films by Raman and infrared spectroscopy. *J. Appl. Phys.* **82**, 5484–5487 (1997). https://doi.org/10.1063/1.365576

[60] Hushur, A., Manghnani, M. H. & Narayan, J. Raman studies of GaN/sapphire thin film heterostructures. *J. Appl. Phys.* **106**, 054317 (2009). https://doi.org/10.1063/1.3213370

[61] Wang, J., Chen, D., Xu, Y., Liu, Q. & Zhang, L. Influence of the crystal texture on Raman spectroscopy of the AlN films prepared by pulse laser deposition. *J. Spectrosc.* **2013**, 103602 (2013). https://doi.org/10.1155/2013/103602

[62] Cai, L. C., Chen, H., Bao, C. L., Huang, Q. & Zhou, J. M. Raman spectroscopic studies of InAs epilayers grown on the GaAs (001) substrates. *J. Cryst. Growth* **253**, 112–116 (2003). https://doi.org/10.1016/S0022-0248(03)01034-0